



**HAL**  
open science

## Various effects of magnetite on international simple glass (ISG) dissolution: implications for the long-term durability of nuclear glasses

Lindsey Neill, S. Gin, Thomas Ducasse, Trilce de Echave, Maxime Fournier,  
Patrick Jollivet, Alkiviadis Gourgiotis, Nathalie Wall

### ► To cite this version:

Lindsey Neill, S. Gin, Thomas Ducasse, Trilce de Echave, Maxime Fournier, et al.. Various effects of magnetite on international simple glass (ISG) dissolution: implications for the long-term durability of nuclear glasses. *npj Materials Degradation*, 2017, 1, pp.1. 10.1038/s41529-017-0001-6 . cea-02380473

**HAL Id: cea-02380473**

**<https://cea.hal.science/cea-02380473v1>**

Submitted on 26 Nov 2019

**HAL** is a multi-disciplinary open access archive for the deposit and dissemination of scientific research documents, whether they are published or not. The documents may come from teaching and research institutions in France or abroad, or from public or private research centers.

L'archive ouverte pluridisciplinaire **HAL**, est destinée au dépôt et à la diffusion de documents scientifiques de niveau recherche, publiés ou non, émanant des établissements d'enseignement et de recherche français ou étrangers, des laboratoires publics ou privés.



Distributed under a Creative Commons Attribution 4.0 International License

1 **Various effects of magnetite on ISG glass dissolution: implication for the**  
2 **long-term durability of nuclear glasses**

3 Lindsey Neill<sup>a</sup>, Stéphane Gin<sup>b</sup>, Thomas Ducasse<sup>b</sup>, Trilce De Echave<sup>b</sup>, Patrick Jollivet<sup>b</sup>, Nathalie  
4 A. Wall<sup>a</sup>

5 <sup>a</sup>Chemistry Department, Washington State University, Pullman, WA 99163, USA

6 <sup>b</sup>CEA Marcoule, DTCD SECM, F-30207 Bagnols-sur-Cèze, France

7 Corresponding Authors: S. Gin: [stephane.gin@cea.fr](mailto:stephane.gin@cea.fr); N.A. Wall: [nawall@wsu.edu](mailto:nawall@wsu.edu)

8 **Abstract**

9 Understanding the effect of near-field materials such as iron corrosion products on the alteration  
10 of vitreous nuclear waste is essential for modeling long-term stability of these waste forms in a  
11 geological repository. Monoliths with polished and as cut sides of International Simple Glass  
12 (ISG) – a six oxide borosilicate glass – were altered for 70 days in oxic conditions at 90 °C in a  
13 solution initially saturated in <sup>29</sup>SiO<sub>2</sub> at pH 7; magnetite was then added to the leaching  
14 environment. Solution and solid analysis were performed to correlate the changes in the surface  
15 features and dissolution kinetics. It was found for the first time that magnetite primarily  
16 influences the mechanically constrained surface of the non-polished sides of the monoliths with  
17 little to no effect on the polished surfaces. This highlights the importance of the unique  
18 chemistry within cracks that invokes a drastic change in alteration from glass altered in  
19 environments containing iron corrosion products.

20 **Keywords**

21 Glass alteration; corrosion products; alteration layer; iron; magnetite; surface cracks

22

## 23 Introduction

24 Confinement within a borosilicate glass matrix is the currently proposed method of disposal  
25 of radionuclides remaining from used nuclear fuel from power reactors <sup>1</sup>. In France, the glass  
26 with about 18 wt% of waste is poured in a stainless steel canister. Before being disposed in a  
27 deep geological formation, the canister will be placed into a carbon steel over pack of a few cm  
28 thick <sup>2</sup>. A better understanding the interactions between glass and iron and iron corrosion  
29 products, is necessary to assess the performance of these waste forms and model the source  
30 term <sup>3</sup>.

31 Over the last several decades, work has been performed to understand the fundamental  
32 mechanisms that control the glass dissolution process under a variety of conditions, and to link  
33 these mechanisms to the global kinetics <sup>4</sup>. The processes that control glass dissolution in a  
34 geological repository involve a complex set of reactions whose importance tremendously  
35 depends on the nature of the host rock, the near field materials <sup>5,6</sup>, the temperature and the  
36 ground water composition and renewal rate, along with the glass composition <sup>7-13</sup>. The ultimate  
37 goal to parametric studies of glass alteration under a variety of conditions is build a predictive  
38 model that can account for the kinetics of long-term alteration <sup>14-16</sup>. Since experimental  
39 validation of the predictive models under accelerated conditions is not possible as glass  
40 dissolution is controlled by coupled non linear processes (Poinssot and Gin JNM), validation  
41 relies on the study of archeological and basaltic glasses <sup>17-19</sup>. A thorough understanding of all  
42 mechanisms and kinetics must be achieved to build a robust model.

43 Literature pertaining to borosilicate glass dissolution demonstrates that silica species play a  
44 large role in the mechanisms and associated kinetics. In diluted conditions water begins to  
45 diffuse into the glass matrix (hydration) <sup>20</sup> and alkali ions begin to exchange with the positively  
46 charged hydrogen species (interdiffusion) <sup>21-23</sup> (equation 1). Hydrolysis of the silicon network

47 also begins with silica being released into solution <sup>24,25</sup> (equation 2 and 3). The corresponding  
48 kinetic regime is designated as the *initial* or *forward rate* and is denoted by  $r_0$ .



49

50 As the silica concentration in solution increases, the rate slows into a *residual rate*  
51 denoted by  $r_r$ . The decrease in rate is attributed both to the decrease of the affinity of the  
52 reaction of hydrolysis of the silicate network and to the formation of a gel layer that becomes  
53 transport limiting <sup>26</sup>. Two different mechanisms are proposed for the formation of this gel layer.  
54 One is based on the precipitation of a silica rich layer on the glass surface. The second is due to  
55 in-situ recondensation of the silicon oxygen bonds which forms a porous gel layer on the glass  
56 surface. Previous studies have used isotopic tracers to differentiate between these  
57 mechanisms, allowing a greater understanding of the exchange of silicon between the bulk  
58 solution and glass surface <sup>27-30</sup>. These studies showed that only one single mechanism may not  
59 be responsible for the residual rate but a combination of these mechanisms that are heavily  
60 dependent on the solution pH.

61 There is also a possibility of an alteration resumption, commonly attributed to the rapid  
62 precipitation of secondary phases <sup>31</sup>. In this regime, zeolites and calcium silicate hydrates form  
63 at the expense of the passivating film. Additionally, environmental complexants, such as organic  
64 molecules or iron corrosion products, can have detrimental effects on the passivating layer <sup>32,33</sup>.  
65 Glass compositions, such as those high in aluminum, and solution pH are two key factors  
66 controlling this regime <sup>34</sup>.

67           Some of the above listed mechanisms are still under investigation, especially at small  
68 scale following the aim to link the basic mechanisms to the three main kinetic regimes (initial  
69 rate, residual rate, resumption of alteration)<sup>4</sup>. As said above, many factors can influence the  
70 kinetics such as pH, temperature, solution conditions, and environmental factors (i.e. near-field  
71 materials<sup>35</sup>).

72           Iron and the associated corrosion products (mainly siderite and magnetite<sup>36</sup> have been  
73 seen to enhance glass alteration both by the sorption of silica onto the surface of the iron-rich  
74 phases and by the precipitation of iron silicate<sup>37-42</sup>. Each of these different processes disturbs  
75 the equilibrium established between the glass surface layers and surrounding solution; these  
76 processes contribute to higher alteration rates for times depending on the amount and  
77 availability of iron in vicinity of the glass.

78           In addition to the processes listed above (sorption of silica on iron corrosion products  
79 and precipitation of iron silicates),<sup>33</sup> studied the effects of magnetite on SON68 glass – the  
80 French high level waste reference glass – and suggested that two other processes might take  
81 place: 1) precipitation of SiO<sub>2</sub> on the magnetite surface and 2) iron incorporation into the glass  
82 alteration layers with potential modifications of their transport properties. The present study  
83 gave evidence to each processes listed above except iron incorporation into the alteration layer  
84 which would be highly dependent on the iron available in solution due to dissolution of the  
85 magnetite. This demonstrates that the iron – glass relationship is complex and that much more  
86 information to understand these effects both on mechanisms and kinetics are needed.

87           Another factor that contributes to the durability of the glass is the formation of cracks on  
88 the glass surface, primarily because cracks increase the reactive surface area compare to a flat  
89 surface. The molten glass is poured into a stainless steel canister after the vitrification process.  
90 As the glass cools, cracks appear because of thermic shock due to a temperature gradient  
91 between the perimeter and core of the glass. At small scale, these cracks or defaults provide

92 preferential sites for alteration such as diffusion of alkali ions into the surrounding environment  
93 <sup>43</sup>

94 At laboratory scale, defaults within the glass matrix are also observed during cooling and  
95 sample preparation (e.g. cutting) <sup>44,45</sup>. These processes can be considered mechanically violent  
96 and generates a high number of micro cracks, or Griffith cracks <sup>46</sup> due to the metastable nature  
97 of the glass structure. Griffith summarized that the strength of the material was dependent on  
98 defects such as these surface cracks. These Griffith cracks can spontaneously propagate in  
99 time due to mechanical stress, chemical gradients, etc. The evolution of these micro cracks into  
100 larger cracks can be compared to dislocations in crystals due to grain boundaries. One method  
101 to remove these sample preparation artifacts is to use soft abrasion in the form of chemically  
102 polishing the glass surface. Though the types of defaults or surface cracks are caused by  
103 different methods, formation vs. processing, looking at alteration of non-polished glass surfaces  
104 can give insight into the alteration of the cracks seen in large-scale waste materials.

105 The goal of this study is to further understand the alteration of the glass waste form in  
106 the presence of iron corrosion products, specifically magnetite (Fe(II,III)Oxide). This study is an  
107 extension of a similar experiment performed. Experimental conditions of both works are similar,  
108 but the present work includes the addition of an iron source <sup>28</sup>. Comparison of results of this  
109 work with a reference experiment without an iron source, allows for a better understanding of  
110 the alteration layer properties. The experiment was carried out in condition initially saturated in  
111 <sup>29</sup>Si to follow the isotopic exchange of Si between the solution and glass to monitor changes of  
112 the alteration layer. Additionally, five of the six sides of the glass monoliths were left unpolished  
113 which gave insight into the effect of surface cracks on the alteration progress of the glass.

## 114 **Results**

### 115 **Solution Analysis**

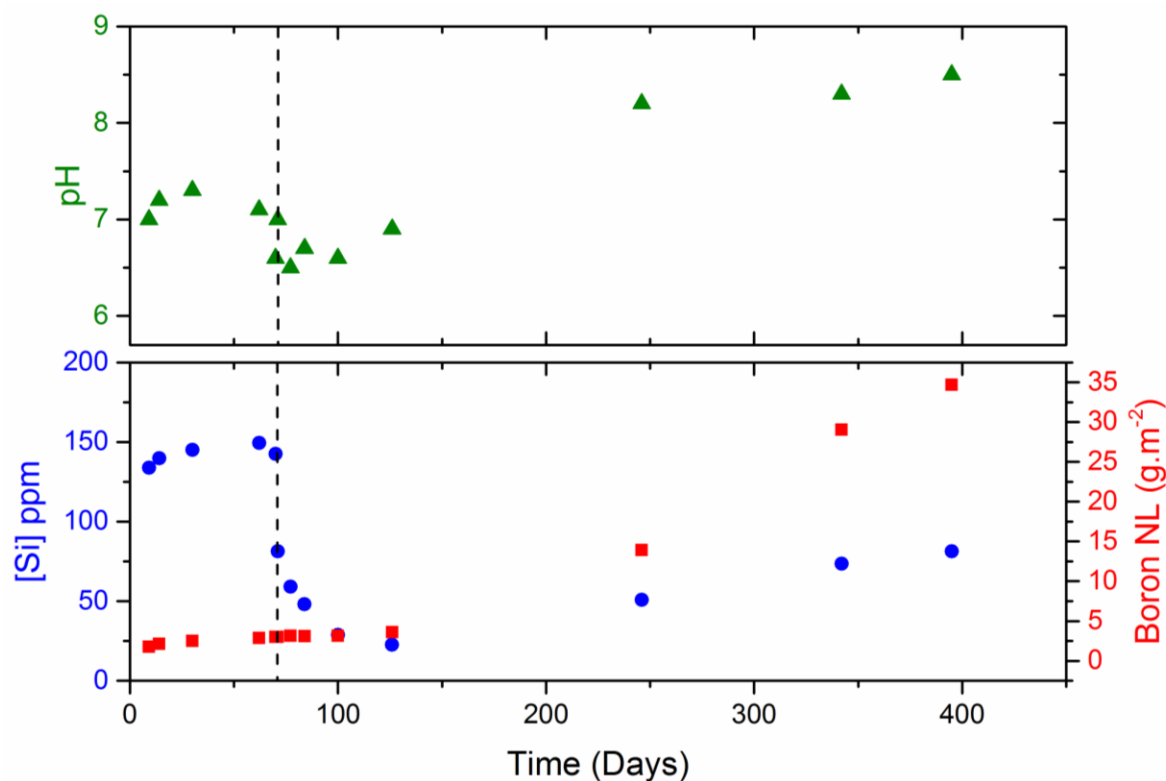
116 Results from ICP-OES for individual glass constitues and MC-ICP-MS for silicon  
 117 isotopes are shown in Table 1.

Time Days	pH <sub>90°C</sub>	AGF %	ICP-OES						MC-ICP-MS			
			Si mg.L <sup>-1</sup>	B mg.L <sup>-1</sup>	Ca mg.L <sup>-1</sup>	Na mg.L <sup>-1</sup>	Fe mg.L <sup>-1</sup>	K g.L <sup>-1</sup>	<sup>28</sup> Si mg.L <sup>-1</sup>	<sup>29</sup> Si mg.L <sup>-1</sup>	<sup>30</sup> Si mg.L <sup>-1</sup>	<sup>101</sup> Si mg.L <sup>-1</sup>
0.4	7.2	0	140.0	<0.1	0.9	6.3	BD	3.5	2.1	135.4	2.4	140.0
9	7.0	0.18	133.8	6.7	5.7	16.7	BD	3.7	-	-	-	-
14	7.2	0.21	139.7	8.1	7.3	20.2	BD	3.8	15.4	122.8	1.5	139.7
30	7.1	0.25	144.9	9.5	6.8	20.8	BD	3.7	16.7	126.7	1.6	144.9
62	7.1	0.29	149.2	10.9	9.2	23.5	BD	3.8	18.0	129.5	1.7	149.2
70	6.6	0.30	142.5	11.6	8.4	25.0	BD	3.0	8.0	133.3	1.3	142.6
71	7.0	0.30	81.2	11.8	12.9	29.7	BD	3.0	7.9	73.1	0.9	81.3
77	6.5	0.32	59.4	12.6	14.7	32.4	BD	2.9	6.7	51.6	0.8	59.1
84	6.7	0.32	48.1	12.6	11.9	32.8	BD	3.0	9.5	37.7	0.8	48.1
100	6.6	0.32	28.7	12.9	10.6	33.8	BD	3.1	7.7	20.4	0.6	28.7
126	6.9	0.37	22.6	15.2	9.8	37.6	BD	3.5	2.3	18.4	0.2	21.0
246	8.2	1.61	50.7	65.3	13.7	121.9	0.06	4.2	27.3	11.8	1.84	40.9
342	8.3	3.37	73.6	126.2	28.2	227.4	BD	3.7	-	-	-	-
395	8.5	4.68	81.3	149.6	29.0	278.8	BD	3.6	-	-	-	-

Table 1: ICP-OES and MC-ICP-MS analysis of solution sampled at various time points. BD indicates that the value for that element was below the 0.1 mg.L<sup>-1</sup> detection limit. Dotted line represents the addition of magnetite 'AGF' stands for Altered Glass Fraction and '-' within the MC-ICP-MS data denotes that the sample was not analyzed at that time point. There is a 10% uncertainty on each element measured by ICP-OES except Na which has a 50% error due to contamination within the K salts used to synthesize the potassium silicates during alkaline fusion. These potassium silicates were used to prepare the initial solution of 150 ppm Si. Elements measured by MC-ICP-MS have a 5% error due to matrix effects. The dotted horizontal line represents the addition of magnetite

118 Figure 1 shows the evolution of the silicon concentration along with the normalized loss based  
 119 on boron solution conditions and pH throughout the experiment. The pH remained constant  
 120 during the 150 first days by monitoring the solution and correcting to pH 7 by 0.5 M HNO<sub>3</sub> or 0.5

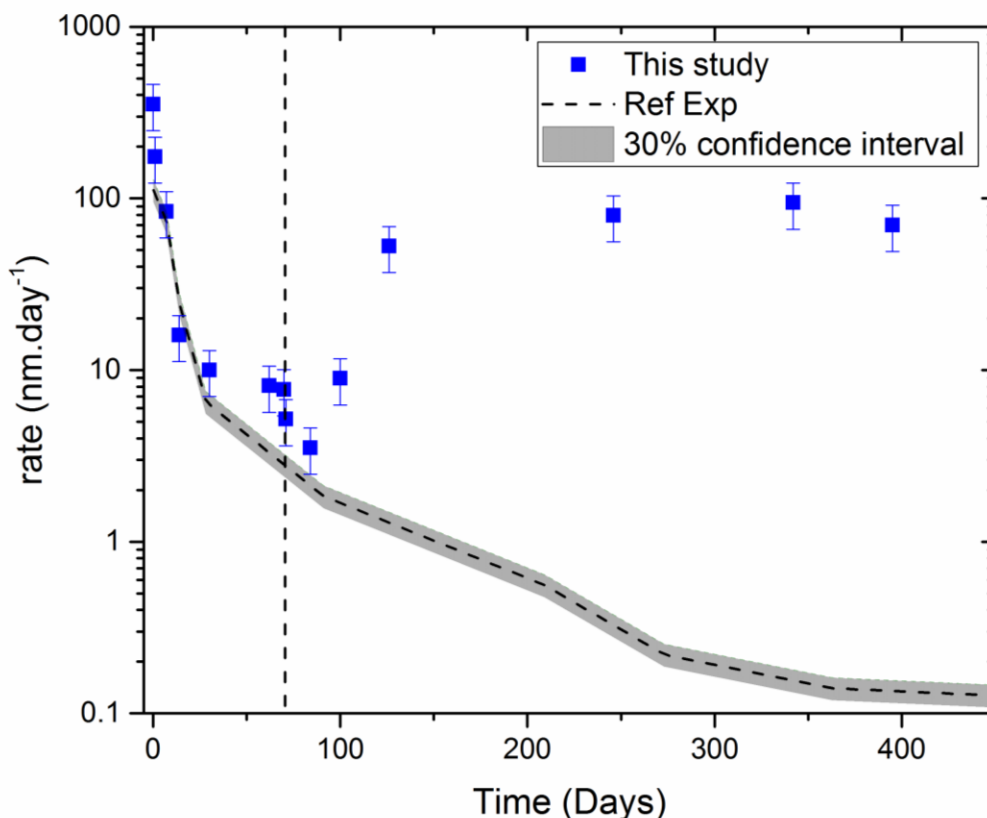
121 M KOH. At the last three time points, the pH slowly increased to approximately 8. Because this  
 122 drift let the pH below orthosilicic acid starts dissociating into anions ( $\text{H}_3\text{SiO}_4^-$ ,  $\text{H}_2\text{SiO}_4^{2-}$ ...), this  
 123 seems to have an insignificant effect on the studied system. Indeed, the glass dissolution rate,  
 124 as shown in figure 2, remains essentially constant between day 126 and day 395.



125  
 126 *Figure 1: Upper graph shows the evolution of the pH (green triangles) during the experiment. At each time point the pH was*  
 127 *corrected back to 7 after the initial measurement shown in the graph except for the last three time points. Lower graph shows*  
 128 *the change in Si concentration (blue circles) and the normalized loss (red squares) calculated by boron concentration in solution.*  
 129 *Resumption of alteration is seen at day 246 based on the increased concentration of boron and silicon in solution.*

130 Over approximately the first two months, the glass was allowed to react in a solution  
 131 saturated with amorphous silica under the same experimental conditions as seen in Gin et al  
 132 2015. This allowed for comparison to a long term study to determine the deviations in behavior  
 133 after magnetite is added to the system. Magnetite was added 70 days after the experiment was  
 134 initiated and a significant decrease in the concentration of silicon was observed almost

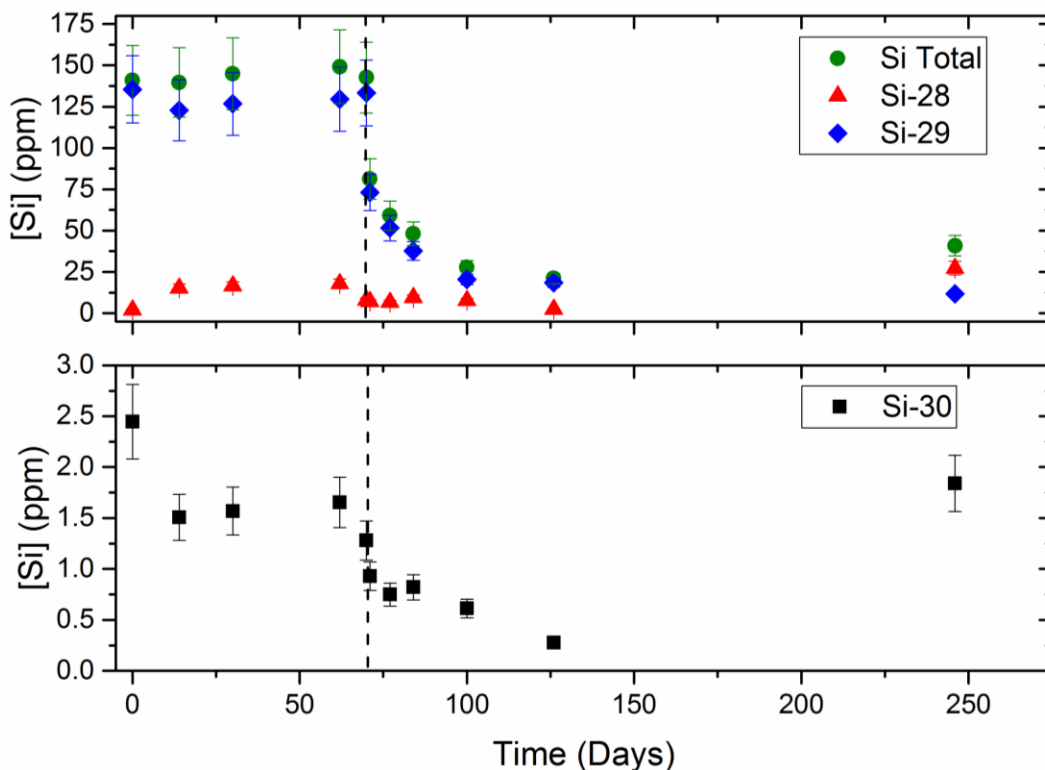
135 immediately with a decrease of approximately 60 ppm of silicon within the first day after  
136 magnetite addition. This decrease extends for two months after the addition of magnetite, at  
137 which point the solution only contains 22 ppm of silicon. The later time points extending to nine  
138 months after the addition of magnetite shows the resumption of alteration. Figure 2 presents the  
139 rate changes over the duration of the experiment based on the boron concentrations in solution.



140  
141 *Figure 2: Rates of alteration calculated based on a linear regression of the equivalent thickness determined at each time point.*  
142 *The grey dotted line represents the rates seen within the reference experiment with a 30% confidence interval (gray shading).*  
143 *The black dotted line represents the addition of magnetite at day 70.*

144 The rate continues to decrease after the addition of magnetite at day 70, although the  
145 rate never reaches the long term rates seen in Gin et al 2015 of 0.1 nm.day<sup>-1</sup>. After ca. 100  
146 days, the rate then increases. The rate then stays to a maximum of around 100 nm.day<sup>-1</sup> for the  
147 duration of the experiment. While this is a large increase, rates near the value calculated at day

148 one of this experiment ( $500 \text{ nm}\cdot\text{day}^{-1}$ ) were not seen even with silicon concentrations under the  
149 saturation value. Silicon isotopic concentrations were also monitored by MC-ICP-MS as shown  
150 in Figure 3.



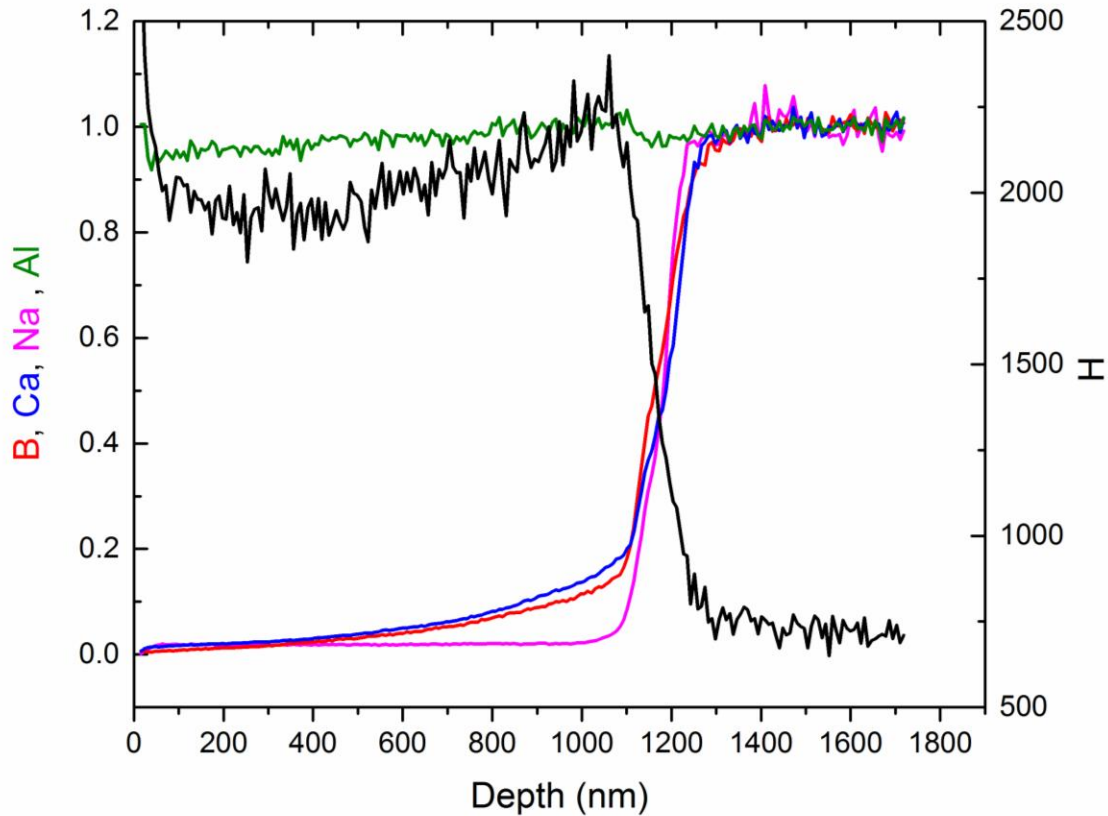
151  
152 *Figure 3: Evolution of Si concentration by isotope determined by analysis of the solution by MC-ICP-MS. The lower graph shows*  
153 *only Si-30 as it makes up less than 1% of the total Si concentration. The dotted black line represents the addition of magnetite at*  
154 *day 70.*

155 Figure 3 demonstrates three different regimes. First, the system is in equilibrium, before  
156 the addition of magnetite, where surface layers form with no or little exchange with Si species  
157 present in the solution, as previously demonstrated<sup>28</sup>. The second regime lasts between days  
158 70 – 126, during which the available Si in solution is consumed, either by sorption or  
159 precipitation on the magnetite surface or iron silicate precipitation. The third regime expands  
160 beyond 126 days. Si concentration increases though only <sup>28</sup>Si and <sup>30</sup>Si increase with <sup>29</sup>Si  
161 continues to decrease. This demonstrates that later time points are a resumption of alteration of

162 the glass itself. If the increased concentrations of Si were due to dissolution of the silicon early  
163 fixed on the magnetite surface, <sup>29</sup>Si concentrations would have risen as well.

### 164 3.1 TOF-SIMS analysis of the glass monoliths

165 In addition to monitoring changes by solution analysis TOF-SIMS was used to  
166 qualitatively evaluate the changes of mobile elements within the alteration layer at four times  
167 throughout the experiment. Monoliths were withdrawn from the solution at day 70 (immediately  
168 before the addition of magnetite), day 84 (two weeks after addition), day 126 (two months after  
169 addition) and day 246 (almost six months after addition). Figure 4 shows the analysis of the  
170 polished face of the day 70 monolith with the three mobile species (B, Na, and Ca) showing  
171 anti-correlation behavior of the hydrous species represented by H. Sodium and calcium are  
172 known to exhibit this sigmoidal profile due to preferential dissolution of these elements, with  
173 similar behavior by boron <sup>28</sup>. While boron may not release by the same mechanisms as the  
174 alkali species, the low activation energy needed to break the B-O bonds (Zapol et al 2013)  
175 allows for the same profile to be seen.

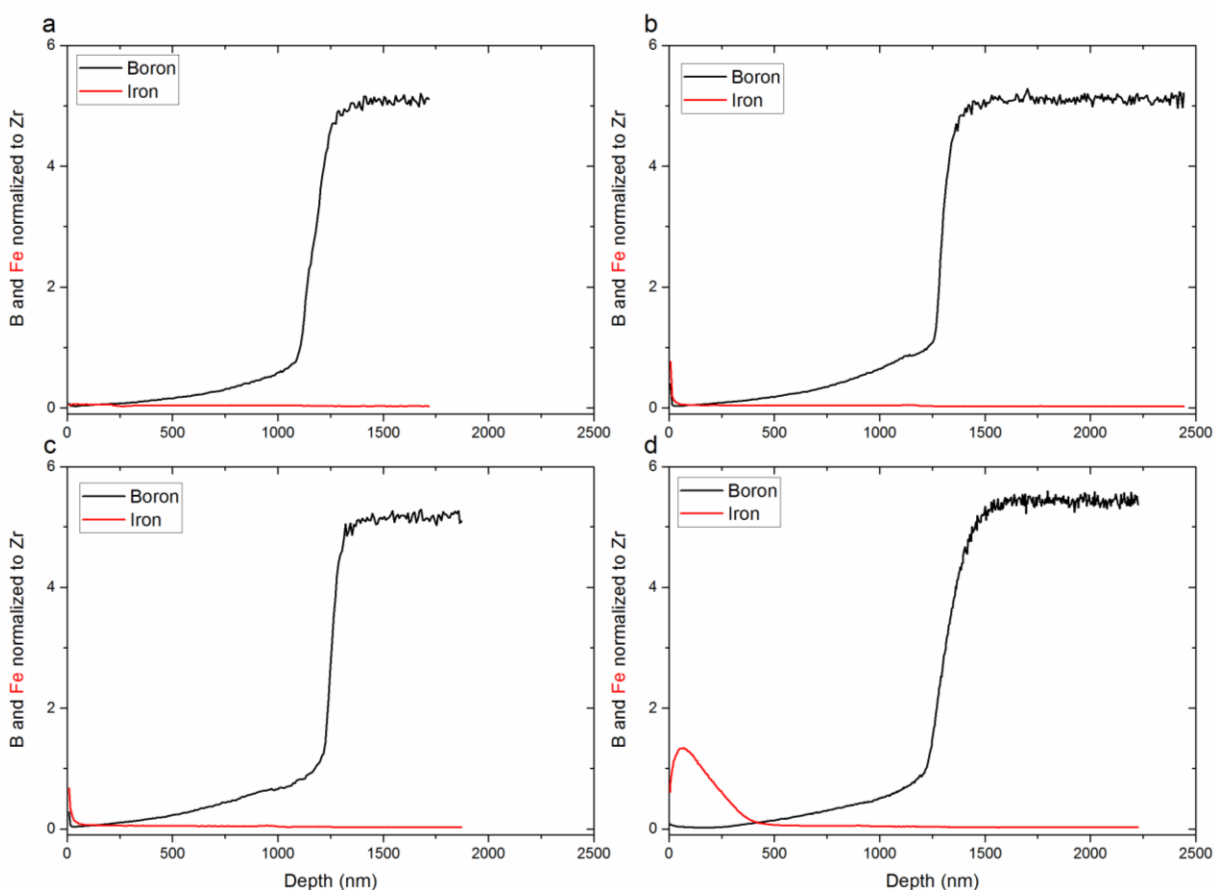


176

177 *Figure 4: TOF-SIMS derived elemental profiles of the major glass constituents of a monolith withdrawn at day 70, right before the*  
 178 *addition of magnetite. This allows for a direct comparison of the monoliths with the reference experiment before the system was*  
 179 *disturbed. All elements, except H, are normalized to Zr as this element is immobile during alteration and to their concentration in*  
 180 *the pristine glass, with allows for a qualitative comparison between the elements.*

181 The potential inclusion of iron into the alteration layers formed on the polished face of  
 182 the monoliths were also studied by TOF-SIMS in Figure 5. Significant iron incorporation into the  
 183 alteration layer is not seen until day 246. Monoliths from day 83 and 126 do show an increase of  
 184 iron within the first couple nanometers of the sample but this could be contributed to magnetite  
 185 grains adhering to the surface instead of being incorporated into the alteration layer. While iron  
 186 containing secondary phases are commonly observed in previous studies, these results suggest  
 187 that iron incorporation happens secondarily to the reactions that occur at the magnetite surface.  
 188 This could also be due to the time it takes for the dissolution of magnetite to introduce iron into

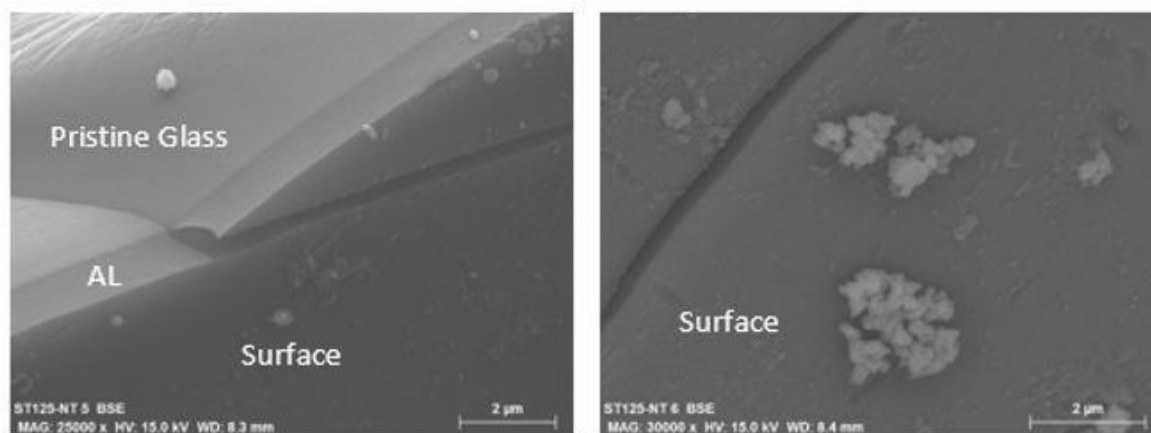
189 the solution since the magnetite and glass surfaces were not in contact. Importantly, these  
 190 profiles also show that there is not a significant increase in alteration layer thickness, based on  
 191 the boron profile, even after the addition of magnetite and calculated resumption of alteration.  
 192 Since only the polished side of the monolith was analyzed by TOF-SIMS, this suggests that the  
 193 behavior of the polished and unpolished sides strongly differ to account for this observation.  
 194 This will be discussed further later in this paper.



195  
 196 *Figure 5: TOF-SIMS elements profiles for iron (red) and boron (black) of the polished surface of each monolith. The boron profile*  
 197 *is shown as a measurement of the alteration layer thickness at each time point. a) day 70: before addition of magnetite*  
 198  *$E_{th} = 1.17 \mu\text{m}$  b) day 83: two weeks after addition  $E_{th} = 1.29 \mu\text{m}$  c) day 126: two months after addition  $E_{th} = 1.25 \mu\text{m}$  d) day 246:*  
 199 *6 months after addition  $E_{th} = 1.26 \mu\text{m}$ . Depths were measured by profilometry during TOF-SIMS analysis.*

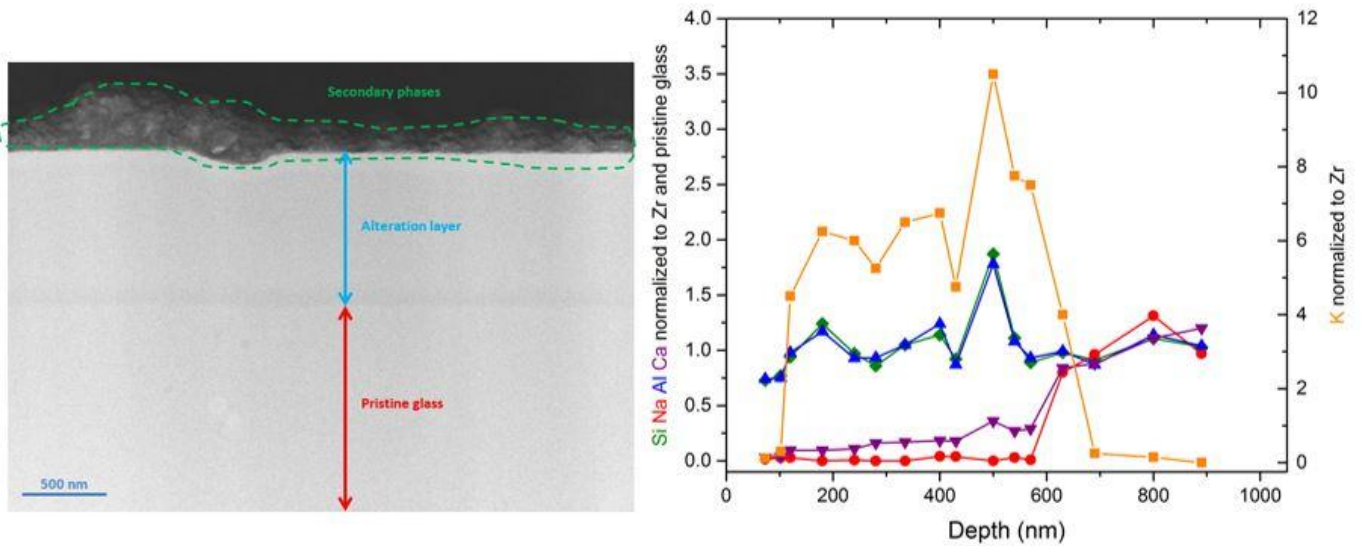
200 **TEM/SEM of glass and magnetite surfaces**

201 Polished faces of the monoliths withdrawn at day 70, 84, and 126 were analyzed by  
202 SEM to monitor the growth of secondary phases and any surface features. The monolith  
203 withdrawn at day 246 was analyzed by TEM. Figure 6 shows images from the day 126 sample  
204 of tilted samples. It was not seen secondary phases on the surface of a monolith until day 126  
205 that EDS and XRD analysis show the secondary phases observed on the 126 day sample are  
206 amorphous and contain elements common to the glass composition. No iron containing  
207 secondary phases were seen at these points in time. In addition to the images displayed in  
208 Figure 7, a cross section of the same monolith was analyzed by SEM to calculate the alteration  
209 layer thickness at this time point (1.26  $\mu\text{m}$ ).



210  
211 *Figure 6: SEM image of polished surface of day 126 monolith. Secondary phases not seen on previous samples have begun to*  
212 *form. Left image shows all three portions of the glass (pristine, alteration layer, and surface). The image on the right shows a*  
213 *close up of the secondary phases seen on the surface.*

214 Figure 7 shows the TEM image of a monolith withdrawn at day 246. This shows an  
215 alteration layer thickness of 1  $\mu\text{m}$  with an additional 300 nm of secondary phases. Electron  
216 diffraction analysis showed that no crystalline phases were present in the alteration layer of the  
217 day 246 monolith. EDS analysis could not identify the secondary phases due to the presence of  
218 large quantities of the deposited metals such as gold and platinum.

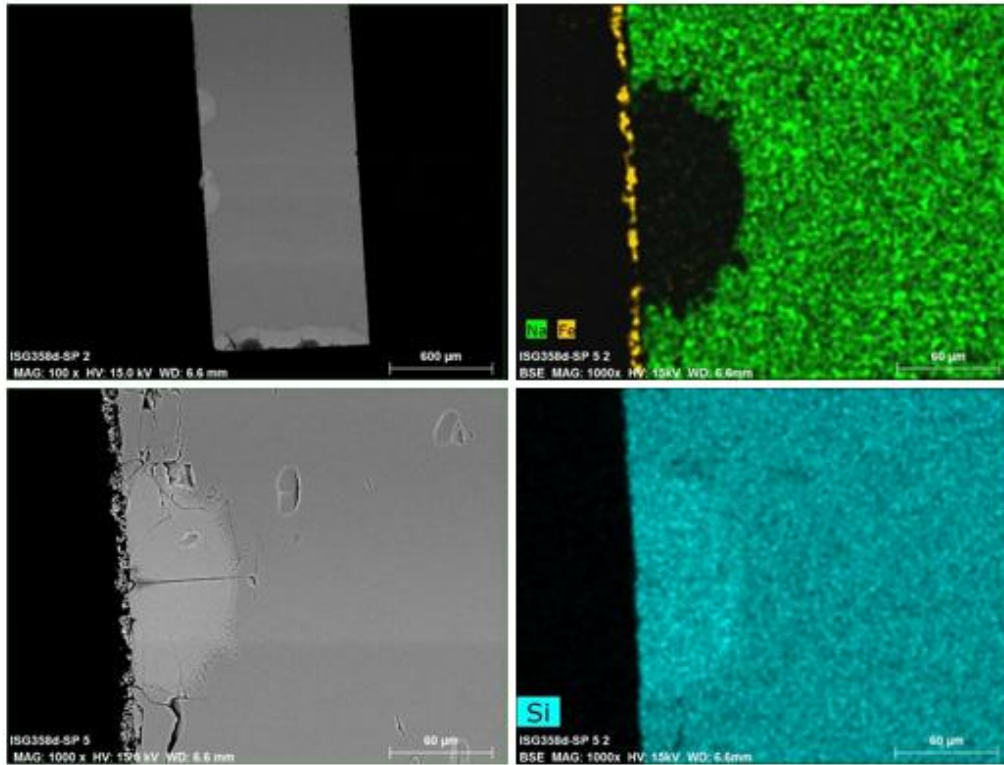


219

220 *Figure 7: TEM image on the left of polished side of day 246 monolith. Alteration layer of approximately 1  $\mu\text{m}$  is seen with an*  
 221 *additional 300 nm of secondary phases on the surface. The absence of contrast inside the alteration layer shows that there is no*  
 222 *porosity yet formed within the alteration layer or that the pore size is inferior to 5 – 10 nm. The right figure shows the EDS*  
 223 *profile of this alteration region.*

224

225 SEM analysis of a monolith withdrawn from the experiment at day 358 showed that  
 226 significant changes at the glass surface happened at the final time point of the experiment.  
 227 Figure 8 shows the alteration layers on the non-polished surfaces of the monolith that now  
 228 contain sections of large amounts of alteration associated with cracks in the glass surface.  
 229 These cracks prove to be a critical feature in the alteration of the glass surface. The majority of  
 230 the alteration takes place primarily at these points instead of a uniform alteration across all  
 231 surfaces as there does not seem to be a change in alteration thickness on the polished surface.  
 232 EDS mapping shows an additional layer containing iron on the glass surface.



233

234 *Figure 8: SEM images of day 358 monolith. In the upper left, the total monolith is shown with the polished side on the right.*

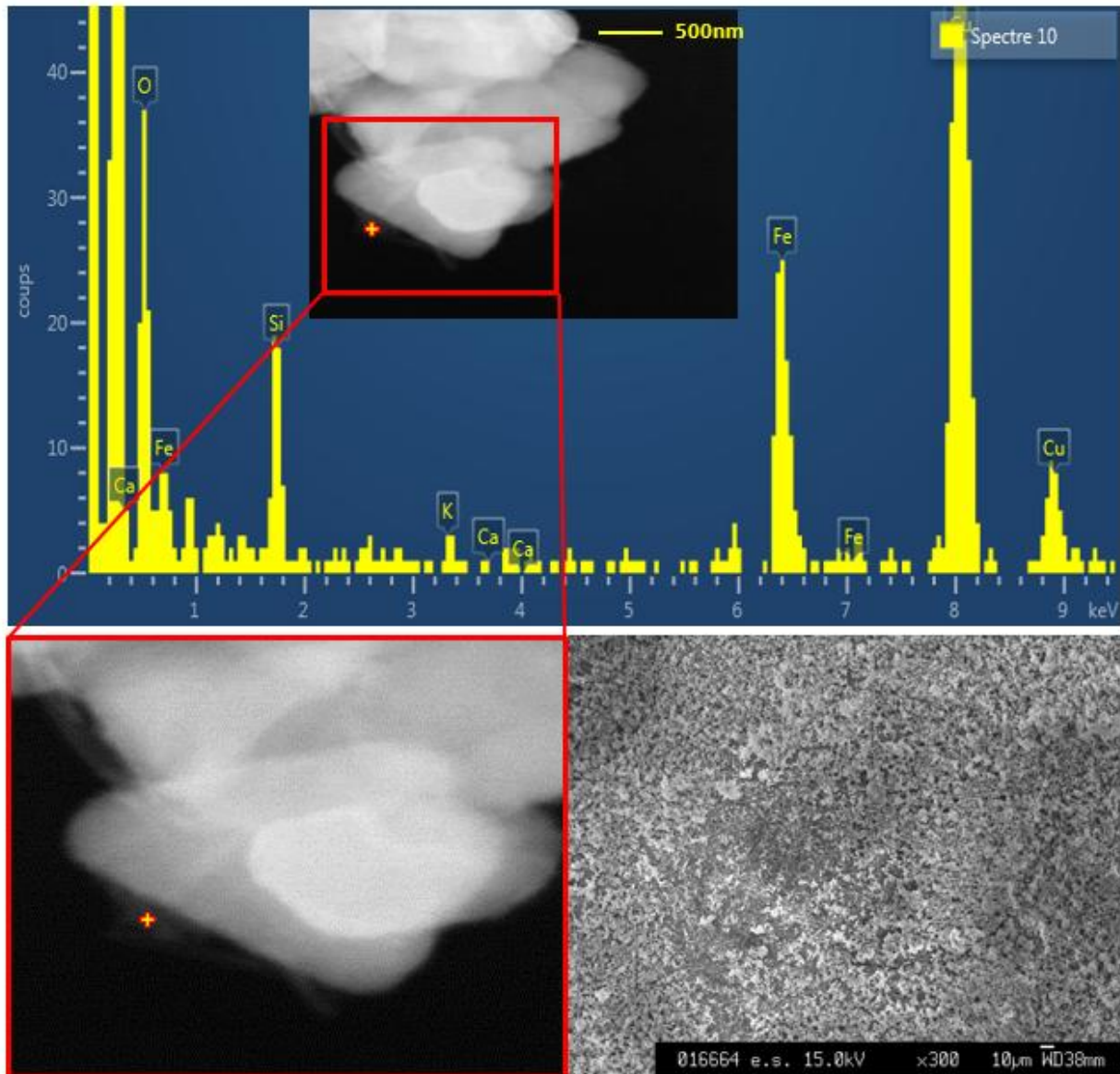
235 *Areas of enhanced alteration are seen on all unpolished surfaces. Bottom left shows a close up of one of these areas of*

236 *alteration that surrounds a crack in the surface. The images on the right show EDS mapping of significant ions denoting the*

237 *alteration area and an iron rich area on the surface that is silicon poor.*

238 TEM and SEM observations were also performed on a sample of magnetite withdrawn at day

239 246; results are presented with Figure 9.



240

241 *Figure 9: TEM image and EDS analysis of one magnetite grain is shown at the top with a zoom of the edge of the magnetite*  
 242 *grain at the bottom left. High concentrations of Cu are seen due to metallic coating during sample preparation. Silicon peaks are*  
 243 *seen along with potassium and calcium which indicate that silicates are precipitating on the surface of the magnetite in addition*  
 244 *to silicon sorption. Bottom right figure shows an SEM image of these silicates covering the surface of the magnetite grain.*

245

246 TEM EDS analysis shows clusters with increased concentrations of silicon outside the grain  
 247 boundary confirming the precipitation of silica or iron silicate on the surface of the magnetite.

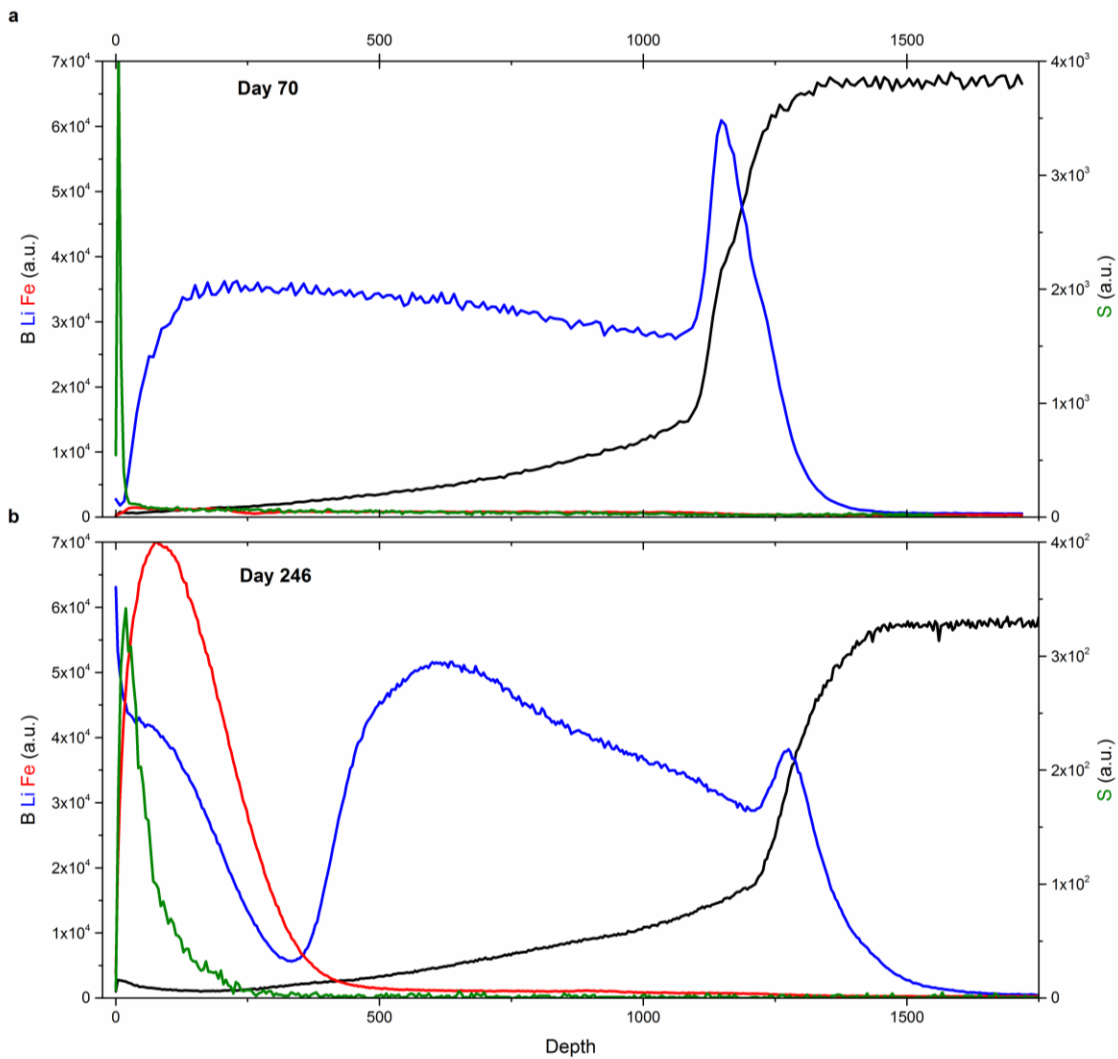
248 SEM images show the entire surface of the magnetite grains is covered with a Si-rich secondary  
249 phase.

250

### 251 **Behavior of diffusive species**

252 In an attempt to further understand the diffusivity changes within the alteration layer formed  
253 on the polished face of monoliths withdrawn at days 70, 84, 126, and 246 were subjected to a  
254 post-tracing experiment as outlined in methods. The behavior of iron into the surface as well as  
255 methylene blue, a molecule of approximately 1 nm in diameter, and Li, which has been shown  
256 to diffuse into the pristine glass at a rate higher than other hydrous species (Neeway et al 2014),  
257 were monitored. Figure 10 shows a comparison of a monolith before the addition of magnetite  
258 and six months after magnetite addition (at which time iron was seen incorporated into the  
259 alteration layer). Since these components are not within the glass composition they cannot be  
260 normalized and thus only give a qualitative view of diffusion into the alteration layers. At day 70,  
261 just before the addition of magnetite, only lithium diffusion is seen suggesting the pores  
262 diameters are too small to allow ingress of large molecules. Methylene blue is seen only within  
263 the first few nm, implying that only molecules of the dye are adhering the outside of the monolith  
264 instead of diffusing into the alteration layers. These results are consistent with those published  
265 in the literature<sup>28,29</sup>. They confirm that a dense layer made of subnanoporous amorphous silica  
266 acts as a molecular sieve for aqueous species. At day 246, two distinct layers are seen; one  
267 with increased iron concentrations and the common alteration layer seen at all time points.  
268 Lithium is seen to partition between these two layers with a decrease at the alteration layer  
269 pristine glass interface while still incorporating into the gel layer and into the pristine glass.  
270 Methylene blue is also present in the secondary iron layer up to the interface of these two  
271 alteration layers. In the reference experiment, methylene blue was also seen to diffuse up to  
272 250 nm of a monolith sampled at day 209. Since this 250 nm cutoff was seen in both the

273 reference experiment and currently with iron introduction, it suggests that iron is not responsible  
 274 for this secondary layer but only this outer 250 nm contain pores with diameters large enough to  
 275 incorporate larger ions. Although there is this significant interface between an iron rich layer and  
 276 the common alteration layer, this is most likely due to the nature of the alteration layer and pore  
 277 diameters of this region instead of an iron affecting the properties or porosity of the alteration  
 278 layer itself.



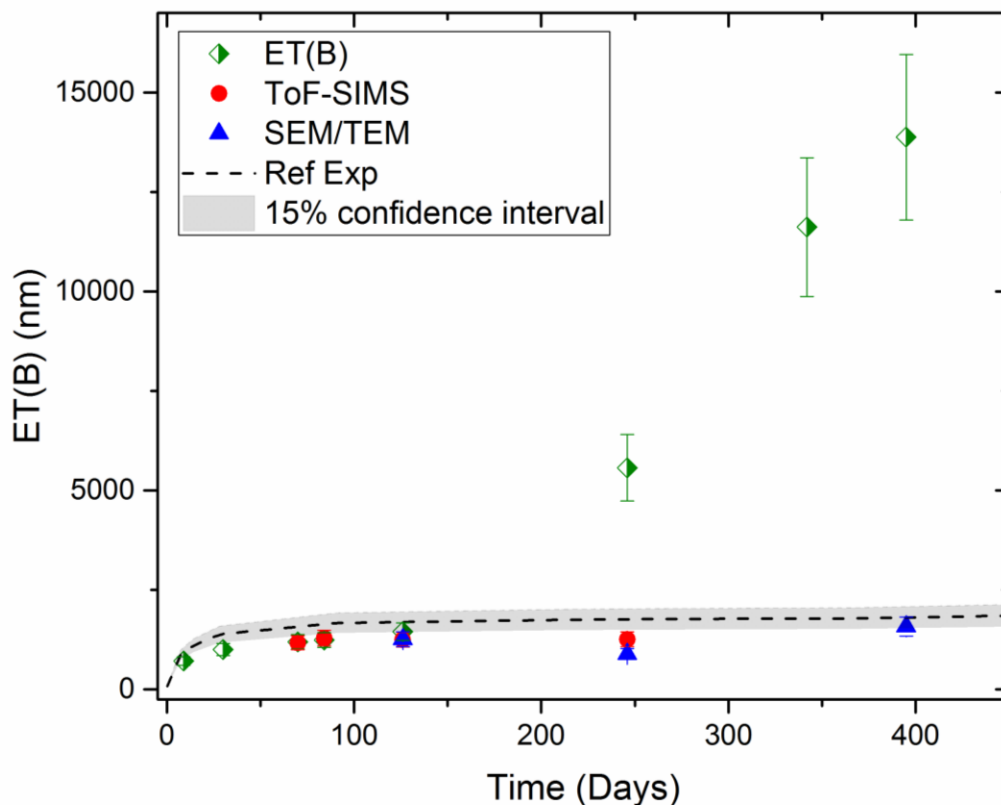
279  
 280 *Figure 10: TOF-SIMS elemental profiles of polished surface of monoliths sampled at a) day 70 and b) day 246 after tracing*  
 281 *experiment with LiCl (Li) and methylene blue (S). Significant changes are seen in the first 250 nm of the day 246 sample.*

282

## 283 Discussion

### 284 Differences in alteration layer thicknesses

285 Analysis the alteration layers by multiple methods demonstrate the inconsistency between  
286 thicknesses derived from boron concentration in solution and those determined by analysis of  
287 the polished side by ToF-SIMS and TEM/SEM measurements. In the reference experiment,  
288 there was a slight increase in values determined by solution determination but values for all  
289 methods were within a 15% uncertainty. With the addition of magnetite a much larger  
290 discrepancy was seen between the methods as shown in Figure 11.



291

292 *Figure 11: Comparison of alteration layer thickness measurements by technique. Agreement within all techniques is seen until*

293 *after alteration resumed. Physical measurements of the polished side of the monolith remain in agreement with the reference*

294 *experiment. Changes determined by increased concentrations of boron in solution highlight the effect of the alteration at*  
295 *surface cracks on the non-polished sides. Dotted line represents the alteration layer thicknesses determined in the reference*  
296 *experiment along with a 15% confidence interval.*

297         The three methods show agreement up until the rate resumption. Even after this time  
298 there is not a significant change in the alteration layer thickness of the polished side that was  
299 analyzed by ToF-SIMS and SEM/TEM; the alteration layer thicknesses remain within error of  
300 the reference experiment even after the resumption of alteration. In similar experiments<sup>28,29</sup> a  
301 correction factor was included to account for the different rate of alteration of the rough non  
302 polished surfaces. This experiment shows the exaggerated effects from these experiments that  
303 did not contain magnetite. It appears that the rough or as cut surfaces show preferential  
304 alteration over the polished side. These reference experiments showed that the non-polished  
305 surfaces contributed to a surface area 1.7x larger than that of just geometric considerations.  
306 This correction is applicable to the first regime in the absence of magnetite. But even factoring  
307 in this difference, it does not explain the factor 15 difference in the thicknesses (up to a factor 70  
308 locally) obtained by solid and solution analysis. Moreover, a slight decrease of silicon  
309 concentration was seen between day 126 and day 246 but since the alteration layer should  
310 already be depleted in boron it does not explain this difference. It was found that the non-  
311 polished side had areas of large alteration that were centered on cracks in the surface that  
312 could begin to explain the discrepancies in thickness measurements.

313

#### 314 **Mechanisms of iron interaction**

315         Many of the mechanisms detailed in Rebiscoul et al 2015 were seen in the work,  
316 although it is difficult to distinguish between Si sorption and SiO<sub>2</sub> precipitation by methods used  
317 in this experiment. It has to be assumed that both of these mechanisms (sorption and  
318 precipitation) were observed since the consumption of Si from solution was higher than can be

319 accounted for by sorption only. The sorption capacity for magnetite has been measured to be 19  
320  $\pm 14$   $\mu\text{mol}$  of Si per gram of magnetite <sup>47</sup>. In this experiment this sorption capacity only allows for  
321 7-80 ppm of Si (allowing for the large error within the measurement provided by Philippini et al)  
322 of the 120 ppm loss seen over the first two months after the addition of magnetite. Since the  
323 mechanisms of sorption and  $\text{SiO}_2$  cannot be separated, it can be speculated that sorption takes  
324 place within the first day after magnetite was added to the system. Approximately 60 ppm of  
325 silica was lost from solution from day 70 to day 71 which falls within the range of 7 – 80 ppm  
326 that can be accounted for by the sorption capacity. Thus, both sorption and  $\text{SiO}_2$  precipitation  
327 mechanisms that occur at the magnetite surface seem to predominate in the initial stages with  
328 the formation of secondary phases or a layer of iron at the glass surface seen only at the later  
329 time points in the experiment.

330 In an additional experiment, ISG grains of approximately 5  $\mu\text{m}$  in diameter were altered  
331 in the same conditions as those tested here (pH 7, 90 °C, solution at equilibrium with  
332 amorphous silica) until 100% of boron had been released (complete alteration of the glass  
333 grains). This left grains that can be thought of as pure alteration layer. The solubility of these  
334 altered grains were then measured, and after 100 days the system reached an equilibrium with  
335 a concentration of 43 ppm of Si at pH 7. It can be seen in our data that when the concentration  
336 of Si in this experiment reached levels below this threshold the alteration of the glass surface  
337 resumed. This is also evident from the isotopic concentrations of Si in solution. After this  
338 threshold value of Si was reached, the glass, containing primarily <sup>28</sup>Si, begins to alter to  
339 reestablish the equilibrium in solution; this can be seen with the increase of <sup>28</sup>Si over <sup>29</sup>Si at day  
340 246.

341 Monitoring the diffusion of methylene blue and LiCl also gave insights into if the  
342 incorporation of exogenous elements such as iron changed the properties of the alteration layer.  
343 It is possible that the introduction of iron into the alteration layer could reduce the porosity of the

344 alteration layer and thus affect the ability of ions to diffuse. The GRAAL model predicts that the  
345 durability glass waste form is tied the thermodynamic stability the transport properties of the  
346 passivating layer <sup>14</sup>. While we know that iron is detrimental to the durability glass, a layer that  
347 would restrict iron diffusion would be considered protective over time. But as shown in figure 11,  
348 the iron rich layer did not limit the ability of small ions, Li in this case, to diffuse up and into the  
349 pristine glass layer. Thus under these conditions, iron only decreases the stability of the system  
350 without providing any protective effect.

### 351 **Effects of surface cracks**

352 As discussed above there is a large difference seen in the calculated alteration layer  
353 thickness by boron released and observed on the monolith. This was due to the propagation of  
354 alteration within the cracks on the rough surfaces, a phenomenon that was unexpected when  
355 this study was designed. While the alteration layer on the polished side remained the same  
356 thickness as seen in the experiment conducted by Gin et al 2015 of approximately 1  $\mu\text{m}$ , the  
357 zones of alteration around the cracks extended up to 60 – 70  $\mu\text{m}$  as shown in Figure 8. The  
358 effects of these cracks must carefully be considered since actual waste packages are expected  
359 to have many cracks due to cooling of the glass and any possible stress fractures from  
360 movement of the canister <sup>48</sup>. Though cracks within glass have been studied though not many  
361 studies have been directly related to nuclear glasses under repository conditions <sup>48,49</sup>. These  
362 cracks substantially increase the surface area of the glass block along with providing areas with  
363 unique chemical environments. The localized conditions within these cracks provide a  
364 preferential site for quick alteration.

365 Stress fractures on the rough surfaces of the monoliths were also seen in the reference  
366 experiment <sup>28</sup> yet alteration progressed quicker when in the presence of magnetite than seen  
367 previously. This could be due to the quick change in solution conditions when magnetite was  
368 added to the system. Within the first two months after the addition of magnetite the

369 concentration on silicon decreased from a steady state of about 140 ppm to around 20 ppm with  
370 a decrease in 60 ppm seen in the first day. This extreme change in solutions caused the  
371 resumption of alteration and it was the surface cracks that provided sites for this alteration to  
372 reestablish the equilibrium between solution and the glass matrix.

373 Several studies have shown that unique chemical environments exist within these  
374 cracks.<sup>50,51</sup> showed that there is an increase in diffusion constants of ions, specifically Na,  
375 within the cracks as compared to the bulk glass. The diffusion of these ions also creates a  
376 condensate region at the surface of the glass around the cracks. The pH in these regions  
377 increases compared to bulk solution which can lead to regions of increased silicate ion  
378 formation due to hydrolysis<sup>52</sup>. So it is not specific to glasses in contact with iron that these  
379 cracks form, but the iron can take advantage of these areas with unique chemistry as compared  
380 to the bulk which facilitates large regions of alteration that were not seen on the time scale of  
381 the reference experiment. Since the rate of propagation increases with the increase in crack  
382 length<sup>53</sup> the formation of these areas could be detrimental to the overall durability of the bulk  
383 glass.

## 384 **Methods**

### 385 **Experimental Set-up**

386 The ISG glass was prepared by MoSci Corporation (Rollo, MO, USA). The composition is given  
387 in Table 1.

388

389

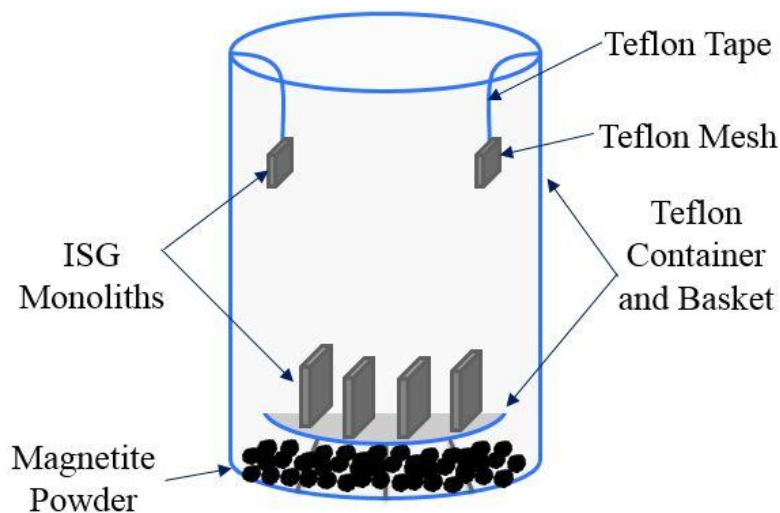
390

Oxide	Wt %	
SiO <sub>2</sub>	56.2	392
B <sub>2</sub> O <sub>3</sub>	17.3	
Na <sub>2</sub> O	12.2	
Al <sub>2</sub> O <sub>3</sub>	6.1	
CaO	5.0	395
ZrO <sub>2</sub>	3.3	

397

Table 2: Composition of ISG  
398

399           The glass was initially melted into ingots using platinum-rhodium crucibles at 1300 °C for  
400 about 4 hours. The ingots were then annealed for 6 hours at 569 °C then cooled to room  
401 temperature at a rate of 50 °C per hour. From one ingot, 8 monoliths of 2.00 x 2.00 x 0.11 cm<sup>3</sup>  
402 and 8 monoliths of 0.50 x 0.50 x 0.11 cm<sup>3</sup> were obtained. One of the large faces of the  
403 monoliths were then polished to a mirror finish. The 8 large monoliths were put into a Teflon  
404 holder and placed in the bottom of a 250 mL Teflon vessel in a vertical orientation. The smaller  
405 monoliths were wrapped in Teflon mesh and hung into solution from the top of the vessel as  
406 shown in Figure 12.



407

408 *Figure 12: Schematic of experimental set - up. Magnetite powder was added into the vessel at day 70.*

409 The initial solution was saturated in amorphous  $^{29}\text{SiO}_2$  (Eurisotop > 95%  $^{29}\text{SiO}_2$ ) at  $\text{pH}_{90^\circ\text{C}}$   
 410 7. The isotopically tagged silica was melted with KOH (Suprapur) at  $600^\circ\text{C}$  and the resulting  
 411 soluble potassium silicate was then dissolved in  $18 \text{ M}\Omega\cdot\text{cm H}_2\text{O}$  to obtain a concentration of 141  
 412 ppm Si and 6900 ppm K. Due to a small initial concentration of additional cations (i.e. sodium  
 413 and calcium) an aliquot of the initial solution was characterized by Inductively Coupled Plasma  
 414 Optical Emission Spectroscopy (ICP-OES) for consideration of further calculations.

415 The resulting surface area was  $76 \text{ cm}^2$  by geometric considerations. A previous study  
 416 has found that the resulting reactive surface area due to only one polished face of the monolith  
 417 is 1.7 x higher than the geometric surface area <sup>29</sup>; the resulting reactive SA was  $129 \text{ cm}^2$ . The  
 418 smaller monoliths contribute only a small fraction of the SA so these monoliths are used for  
 419 sampling throughout the experiment. The  $\text{pH}_{90^\circ\text{C}}$  of the solution was maintained at  $7.0 \pm 0.5$  by  
 420  $0.5 \text{ M KOH}$  and  $0.5 \text{ M HNO}_3$ , and  $90^\circ\text{C}$ , until around 6 months and was then let free to vary.

421 As the leaching solution was initially saturated with respect to amorphous silica, the  
422 glass was altered in a residual rate until day 70 at which time the system was perturbed.  
423 Approximately 9.3 g of magnetite (Sigma Aldrich 0.48  $\mu\text{m}$  average particle size) was added.

#### 424 **Solution Analysis**

425 The solution was sampled regularly throughout the experiment for cation concentrations  
426 analysis by ICP-OES and silicon isotope ratios by ICP-MS. All samples and standards were  
427 purified using BioRad AG50 X-12 (200-400 mesh) cation exchange resin before silicon isotope  
428 analysis, as described in detail by Georg et al <sup>54</sup>. Silicon isotope ratio measurements were  
429 performed on a Thermo Scientific Neptune Plus Multi-Collector Inductively Coupled Plasma  
430 Mass-Spectrometer (MC-ICPMS) at the Institut de Physique du Globe de Paris, France. All  
431 measurements were performed in static multicollection mode with Faraday cups attached to  
432  $10^{11} \Omega$  amplifier resistors. The Faraday amplifier gains were calibrated daily before the analytical  
433 session, yielding long-term reproducibility better than 10 ppm. The instrument was operated at  
434 medium resolution to avoid polyatomic interferences (e.g.  $^{14}\text{N}^{16}\text{O}$ ,  $^{14}\text{N}_2$ ,  $^{12}\text{C}^{16}\text{O}$ ) (Savage et al.  
435 2013, Supplementary Material). The isotope beams of  $^{28}\text{Si}$ ,  $^{29}\text{Si}$  and  $^{30}\text{Si}$  were measured using  
436 L3, C and H3 cups, respectively. A tandem cyclone-Scott type spray chamber SIS (Stable  
437 Introduction System, Thermo Scientific) with a PFA micro-flow nebulizer (ESI, USA) was used  
438 as the introduction system.

439 Boron solution concentrations were obtained by ICP-OES and were used to calculate  
440 the normalized loss (NL), the equivalent thickness (*Eth*) and subsequent rates (*r*) along with the  
441 altered glass fraction (AGF). The calculation for normalized loss is shown in equation 4.

$$NL(B) = \frac{C_B \times V_{solution}}{((SA_{small} \times n_{small}) + (SA_{large} \times n_{large})) \times f_B} \quad \text{Equation 4}$$

442 Where  $C_B$  is the concentration of boron in solution,  $V$  is the volume of solution,  $\rho$  is the density  
443 of glass which is  $2.5 \text{ g.cm}^{-3}$ ,  $SA$  is the surface area of the glass,  $n$  is the number of monoliths

444 remaining, and  $f_B$  is the fraction of boron in the glass (0.0537). The surface area and volume  
445 values were changed throughout the experiment as monoliths were sampled and correcting for  
446 any evaporation in the system. The equivalent thickness calculation is shown in equation 5  
447 which is the normalized loss divided by the density  $\rho_{\text{glass}}$ .

$$Eth(B) = \frac{NL(B)}{\rho_{\text{glass}}} \quad \text{Equation 5}$$

448 The glass dissolution rate is then calculated as shown in equation 6. This is determined by  
449 using a three point linear regression.

$$r = \frac{d(Eth(B))}{dt} \quad \text{Equation 6}$$

450

451 The altered glass fraction (AGF) is determined by equation 7.

$$AGF = \frac{C_B}{f_B \times (V_{\text{glass}} \times \rho_{\text{glass}})} \quad \text{Equation 7}$$

452 Where  $C_B$  is the concentration of boron in solution in g,  $f_B$  is the fraction of boron in the glass  
453 (0.0537) and  $V_{\text{glass}}$  is the addition of volume from each glass monolith in  $\text{cm}^3$ .

454 The associated uncertainties for  $NL$  is 10%,  $Eth$  is 15%, while  $r$  is 30%.

455 The surface area is that the geometric surface area alone does not take into account the  
456 physical surface area of the monolith. A factor of 1.7x the geometric surface area is used to  
457 correct for surface roughness of the unpolished surfaces for the calculation of surface area of  
458 each monolith<sup>29</sup>, as previously explained. Additionally, the propagation of cracks on the  
459 unpolished surfaces of the monolith provided additional water accessible areas that impact the  
460 overall alteration of the glass monolith. The phenomenon of alteration within these cracks will be  
461 discussed at greater depth within this paper.

462 Monoliths were sampled at multiple times throughout the experiment; day 70 (before  
463 addition of magnetite, day 83 (approx. 2 weeks after addition), day 126 (approx. 2 months after  
464 addition), day 246 (approx. 6 months after addition) and day 358 (approximately 9.5 months  
465 after addition). These monoliths were cut into four pieces for different analyses.

466 The polished face of the first four monoliths were analyzed by TOF-SIMS (IONTOF TOF  
467 5) to visualize elemental profiles within the alteration layer. Two sputtering beams were used  
468  $O_2^+$  (50 x50  $\mu m^2$  area) or  $Cs^+$  (40 x 40  $\mu m^2$  area). The  $Cs^+$  beam was used to analyze the H, and  
469 S ions while  $O_2^+$  was used for all other ions. To minimize the matrix effects, all ions are  
470 normalized to Zr as this element is immobile during alteration <sup>55</sup>.

471 The day 246 monolith was also analyzed by TEM. A thin section was extracted from the  
472 polished face of the sample and milled up to a thickness of ~100 nm. The sample was sputtered  
473 with an Au/Pd mixture and coated with Pt for protection. Observations and analyses were  
474 carried out with a Technai G2 (FEI) TEM microscope equipped with a LaB6 source operating at  
475 200kV. A GATAN CCD camera, a BF-DF detector and an EDX detector EDAX Genesis were  
476 used. The spatial resolution was 0.27 nm and the EDS spot size of 5 and 10 nm. For EDX  
477 analysis, the sample was tilted of 20° to minimize the overlaying of different phases. The  
478 counting time was 20 seconds to limit evaporation of mobile elements. SEM-EDS (JEOL JXA-  
479 8500 F) was also used to observe the alteration layers and surface features of the day-126  
480 (polished face) and the day-358 (as cut face) monoliths.

481 A post-experiment tracing was performed on the monoliths withdrawn at day 70, 83,126,  
482 and 246. The monoliths were placed in a saturated amorphous  $^{28}SiO_2$  at pH 7 at room  
483 temperature for 100 hours. The solution also contained  $4.4 \times 10^{-4} \text{ mol.L}^{-1}$  methylene blue and  
484  $0.1 \text{ mol.L}^{-1}$  LiCl. TOF-SIMS was performed on the polished face of the samples to study the  
485 diffusivity of these aqueous species into the developing alteration layers. This allowed for

486 comparison to the reference sample to further understand the influence of iron on the properties  
487 of the alteration layer.

#### 488 **Acknowledgements**

489 This research was performed using funding received from the DOE Office of Nuclear Energy's  
490 Nuclear Energy University Program under Project 23-3361 in addition to funding provided by the  
491 CEA, Areva, and the Chateaubriand Fellowship from the Embassy of France in the U.S. Authors  
492 warmly thank Alkis Gourgiotis from IRSN, France for MC-ICP-MS analyses, Laurent Dupuy at  
493 Biophy Research, France for the TOF-SIMS analysis, Martiane Cabié at Aix-Marseille  
494 University, France for assistance with TEM, and CEA technical staffs for SEM analyses.

#### 495 **References**

- 496 1. Donald, I. Waste Immobilization in Glass and Ceramic Based Hosts: Radioactive, Toxic and  
497 Hazardous Wastes. (Wiley, 2010).
- 498 2. ANDRA (Agence Nationale pour la gestion des Déchets RAdioactifs). Dossier 2005: Andra research of  
499 the geological disposal of high-level long-lived radioactive waste. Results and perspective. (2005).
- 500 3. Gin, S. et al. An international initiative on long-term behavior of high-level nuclear waste glass.  
501 Mater. Today **16**, 243–248 (2013).
- 502 4. Vienna, J. D., Ryan, J. V., Gin, S. & Inagaki, Y. Current Understanding and Remaining Challenges in  
503 Modeling Long-Term Degradation of Borosilicate Nuclear Waste Glasses. Int. J. Appl. Glass Sci. **4**,  
504 283–294 (2013).
- 505 5. Andriambololona, Z., Godon, N. & Vernaz, E. R7T7 nuclear glass alteration in a saline medium: in situ  
506 experiments in the WIPP project. Appl. Geochem. **7**, 23–32 (1992).
- 507 6. Jollivet, P. et al. Effect of clayey groundwater on the dissolution rate of the simulated nuclear waste  
508 glass SON68. J. Nucl. Mater. **420**, 508–518 (2012).

- 509 7. Fleury, B. et al. Development of an Experimental Design to Investigate the Effects of R7T7 Glass  
510 Composition on the Residual Rate of Alteration. *Procedia Mater. Sci.* **7**, 193–201 (2014).
- 511 8. Frugier, P., Martin, C., Ribet, I., Advocat, T. & Gin, S. The effect of composition on the leaching of  
512 three nuclear waste glasses: R7T7, AVM and VRZ. *J. Nucl. Mater.* **346**, 194–207 (2005).
- 513 9. Gin, S., Beaudoux, X., Angéli, F., Jégou, C. & Godon, N. Effect of composition on the short-term and  
514 long-term dissolution rates of ten borosilicate glasses of increasing complexity from 3 to 30 oxides.  
515 *J. Non-Cryst. Solids* **358**, 2559–2570 (2012).
- 516 10. Jantzen, C. M., Brown, K. G. & Pickett, J. B. Durable Glass for Thousands of Years. *Int. J. Appl. Glass*  
517 *Sci.* **1**, 38–62 (2010).
- 518 11. Pierce, E. M. et al. Experimental determination of the effect of the ratio of B/Al on glass dissolution  
519 along the nepheline (NaAlSiO<sub>4</sub>)–malinkoite (NaBSiO<sub>4</sub>) join. *Geochim. Cosmochim. Acta* **74**, 2634–  
520 2654 (2010).
- 521 12. Pierce, E. M., Rodriguez, E. A., Calligan, L. J., Shaw, W. J. & Pete McGrail, B. An experimental study of  
522 the dissolution rates of simulated aluminoborosilicate waste glasses as a function of pH and  
523 temperature under dilute conditions. *Appl. Geochem.* **23**, 2559–2573 (2008).
- 524 13. Werme, L. O., Hench, L. L., Nogues, J.-L., Odelius, H. & Lodding, A. On the pH dependence of  
525 leaching of nuclear waste glasses. *J. Nucl. Mater.* **116**, 69–77 (1983).
- 526 14. Frugier, P. et al. SON68 nuclear glass dissolution kinetics: Current state of knowledge and basis of  
527 the new GRAAL model. *J. Nucl. Mater.* **380**, 8–21 (2008).
- 528 15. Grambow, B. & Muller, R. First-order dissolution rate law and the role of surface layers in glass  
529 performance assessment. *J. Nucl. Mater.* **298**, 112–124 (2001).
- 530 16. McGrail, B. P., Ebert, W. L., Bakel, A. J. & Peeler, D. K. Measurement of kinetic rate law parameters  
531 on a Na–Ca–Al borosilicate glass for low-activity waste. *J. Nucl. Mater.* **249**, 175–189 (1997).

- 532 17. Libourel, G. et al. The use of natural and archeological analogues for understanding the long-term  
533 behavior of nuclear glasses. *Comptes Rendus Geosci.* **343**, 237–245 (2011).
- 534 18. Parruzot, B., Jollivet, P., Rébiscoul, D. & Gin, S. Long-term alteration of basaltic glass: Mechanisms  
535 and rates. *Geochim. Cosmochim. Acta* **154**, 28–48 (2015).
- 536 19. Verney-Carron, A., Gin, S., Frugier, P. & Libourel, G. Long-term modeling of alteration-transport  
537 coupling: Application to a fractured Roman glass. *Geochim. Cosmochim. Acta* **74**, 2291–2315 (2010).
- 538 20. Doremus, R. H. Interdiffusion of hydrogen and alkali ions in a glass surface. *J. Non-Cryst. Solids* **19**,  
539 137–144 (1975).
- 540 21. Doremus, R. H. Diffusion-controlled reaction of water with glass. *J. Non-Cryst. Solids* **55**, 143–147  
541 (1983).
- 542 22. Boksay, Z., Bouquet, G. & Dobos, S. Diffusion Processes in Surface Layers of Glass. *Phys. Chem. Glas.*  
543 **8**, 140- (1967).
- 544 23. Ojovan, M. I., Pankov, A. & Lee, W. E. The ion exchange phase in corrosion of nuclear waste glasses.  
545 *J. Nucl. Mater.* **358**, 57–68 (2006).
- 546 24. Hench, L. Physical chemistry of glass surfaces. *J. Non Cryst. Solids* **25**, 343–369 (1977).
- 547 25. Techer, I., Advocat, T., Lancelot, J. & Liotard, J. M. Dissolution kinetics of basaltic glasses: control by  
548 solution chemistry and protective effect of the alteration film. *Chem. Geol.* **176**, 235–263 (2001).
- 549 26. Van Iseghem, P. et al. in *Environmental Issues and Waste Management Technologies in the*  
550 *Materials and Nuclear Industries XII* (eds. Cozzi, A. & Ohji, T.) 115–126 (John Wiley & Sons, Inc.,  
551 2009).
- 552 27. Geisler, T. et al. Aqueous corrosion of borosilicate glass under acidic conditions: A new corrosion  
553 mechanism. *J. Non-Cryst. Solids* **356**, 1458–1465 (2010).
- 554 28. Gin, S. et al. Origin and consequences of silicate glass passivation by surface layers. *Nat. Commun.* **6**,  
555 6360 (2015).

- 556 29. Gin, S. et al. The fate of silicon during glass corrosion under alkaline conditions: A mechanistic and  
557 kinetic study with the International Simple Glass. *Geochim. Cosmochim. Acta* **151**, 68–85 (2015).
- 558 30. Valle, N. et al. Elemental and isotopic (Si-29 and O-18) tracing of glass alteration mechanisms.  
559 *Geochim. Cosmochim. Acta* **74**, 3412–3431 (2010).
- 560 31. Fournier, M., Gin, S. & Frugier, P. Resumption of nuclear glass alteration: State of the art. *J. Nucl.*  
561 *Mater.* **448**, 348–363 (2014).
- 562 32. Gin, S., Godon, N., Mestre, J. P., Vernaz, E. Y. & Beaufort, D. Experimental investigation of aqueous  
563 corrosion of R7T7 nuclear glass at 90°C in the presence of organic species. *Appl. Geochem.* **9**, 255–  
564 269 (1994).
- 565 33. Rebiscoul, D. et al. Reactive transport processes occurring during nuclear glass alteration in  
566 presence of magnetite. *Appl. Geochem.* **58**, 26–37 (2015).
- 567 34. Ribet, S. & Gin, S. Role of neoformed phases on the mechanisms controlling the resumption of  
568 SON68 glass alteration in alkaline media. *J. Nucl. Mater.* **324**, 152–164 (2004).
- 569 35. Reiser, J. et al. Glass Corrosion in the Presence of Iron-Bearing Materials and Potential Corrosion  
570 Suppressors. *MRS Proc.* **1744**, (2015).
- 571 36. Bildstein, O., Trotignon, L., Perronnet, M. & Jullien, M. Modelling iron–clay interactions in deep  
572 geological disposal conditions. *Phys. Chem. Earth Parts ABC* **31**, 618–625 (2006).
- 573 37. Burger, E. et al. Impact of iron on nuclear glass alteration in geological repository conditions: A  
574 multiscale approach. *Appl. Geochem.* **31**, 159–170 (2013).
- 575 38. Dillmann, P., Gin, S., Neff, D., Gentaz, L. & Rebiscoul, D. Effect of natural and synthetic iron corrosion  
576 products on silicate glass alteration processes. *Geochim. Cosmochim. Acta* **172**, 287–305 (2016).
- 577 39. Godon, N., Gin, S. & Frugier, P. SON68 Glass Alteration Enhanced by Magnetite. *Procedia Earth*  
578 *Planet. Sci.* **7**, 300–303 (2013).

- 579 40. McVAY, G. L. & Buckwalter, C. Q. Effect of Iron on Waste-Glass Leaching. *J. Am. Ceram. Soc.* **66**, 170–  
580 174 (1983).
- 581 41. Michelin, A. et al. Archeological slag from Glinet: An example of silicate glass altered in an anoxic  
582 iron-rich environment. *Chem. Geol.* **413**, 28–43 (2015).
- 583 42. Michelin, A. et al. Silicate Glass Alteration Enhanced by Iron: Origin and Long-Term Implications.  
584 *Environ. Sci. Technol.* **47**, 750–756 (2013).
- 585 43. Kittel, C. *Introduction to Solid State Physics*. (John Wiley & Sons, Inc., 2005).
- 586 44. Hed, P. & Edwards, D. Optical Glass Fabrication Technology. 2: Relationship Between Surface  
587 Roughness and Subsurface Damage. *Appl. Opt.* **26**, 4677–4680 (1987).
- 588 45. Preston, F. W. The Structure of Abraded Glass Surfaces. *Trans. Opt. Soc.* **23**, 141–164 (1922).
- 589 46. Griffith, A. A. The Phenomena of Rupture and Flow in Solids. *Philos. Trans. R. Soc. Lond. Ser.*  
590 *Contain. Pap. Math. Phys. Character* **221**, 163–198 (1921).
- 591 47. Philippini, V., Naveau, A., Catalette, H. & Leclercq, S. Sorption of silicon on magnetite and other  
592 corrosion products of iron. *J. Nucl. Mater.* **348**, 60–69 (2006).
- 593 48. Mallet, C., Fortin, J., Guéguen, Y. & Bouyer, F. Evolution of the crack network in glass samples  
594 submitted to brittle creep conditions. *Int. J. Fract.* **190**, 111–124 (2014).
- 595 49. Ougier-Simonin, A., Guéguen, Y., Fortin, J., Schubnel, A. & Bouyer, F. Permeability and elastic  
596 properties of cracked glass under pressure. *J. Geophys. Res. Solid Earth* **116**, B07203 (2011).
- 597 50. Celarie, F., Ciccotti, M. & Marlière, C. Stress-enhanced ion diffusion at the vicinity of a crack tip as  
598 evidenced by atomic force microscopy in silicate glasses. *J. Non-Cryst. Solids* **353**, 51–68 (2007).
- 599 51. Wiederhorn, S. M., Guin, J.-P. & Fett, T. The Use of Atomic Force Microscopy to Study Crack Tips in  
600 Glass. *Metall. Mater. Trans. A* **42**, 267–278 (2010).
- 601 52. Wiederhorn, S. M., Fett, T., Guin, J.-P. & Ciccotti, M. Griffith Cracks at the Nanoscale. *Int. J. Appl.*  
602 *Glass Sci.* **4**, 76–86 (2013).

- 603 53. Freiman, S. W., Wiederhorn, S. M. & Mecholsky, J., John J. Environmentally Enhanced Fracture of  
604 Glass: A Historical Perspective. *J. Am. Ceram. Soc.* **92**, 1371–1382 (2009).
- 605 54. Georg, R. B., Reynolds, B. C., Frank, M. & Halliday, A. N. New sample preparation techniques for the  
606 determination of Si isotopic compositions using MC-ICPMS. *Chem. Geol.* **235**, 95–104 (2006).
- 607 55. Cailleteau, C. et al. Insight into silicate-glass corrosion mechanisms. *Nat. Mater.* **7**, 978–983 (2008).
- 608
- 609